

This is an Open Access document downloaded from ORCA, Cardiff University's institutional repository: <https://orca.cardiff.ac.uk/id/eprint/98422/>

This is the author's version of a work that was submitted to / accepted for publication.

Citation for final published version:

Boateng, Isaac Wiafe, Tia, Richard, Adei, Evans, Dzade, Nelson Yaw, Catlow, Charles Richard and De Leeuw, Nora 2017. A DFT+U investigation of hydrogen adsorption on the LaFeO<sub>3</sub> (010) surface. *Physical Chemistry Chemical Physics* 2017 (10) , pp. 7399-7409. 10.1039/C6CP08698E

Publishers page: <http://dx.doi.org/10.1039/C6CP08698E>

Please note:

Changes made as a result of publishing processes such as copy-editing, formatting and page numbers may not be reflected in this version. For the definitive version of this publication, please refer to the published source. You are advised to consult the publisher's version if you wish to cite this paper.

This version is being made available in accordance with publisher policies. See <http://orca.cf.ac.uk/policies.html> for usage policies. Copyright and moral rights for publications made available in ORCA are retained by the copyright holders.



# A DFT+U Investigation of Hydrogen Adsorption on the LaFeO<sub>3</sub> (010) Surface

Isaac W. Boateng,<sup>a</sup> Richard Tia,<sup>a</sup> Evans Adei,<sup>a</sup> Nelson Y. Dzade,<sup>b</sup> C. Richard A. Catlow,<sup>c,d</sup>  
Nora H. de Leeuw<sup>b,c,d</sup>

<sup>a</sup> Department of Chemistry, Kwame Nkrumah University of Science and Technology, Kumasi, Ghana.

<sup>b</sup> Department of Earth Sciences, Utrecht University, Princetonplein 9, 3584 CC, Utrecht, The Netherlands.

<sup>c</sup> Department of Chemistry, University College London, 20 Gordon Street, WC1H 0AJ, UK

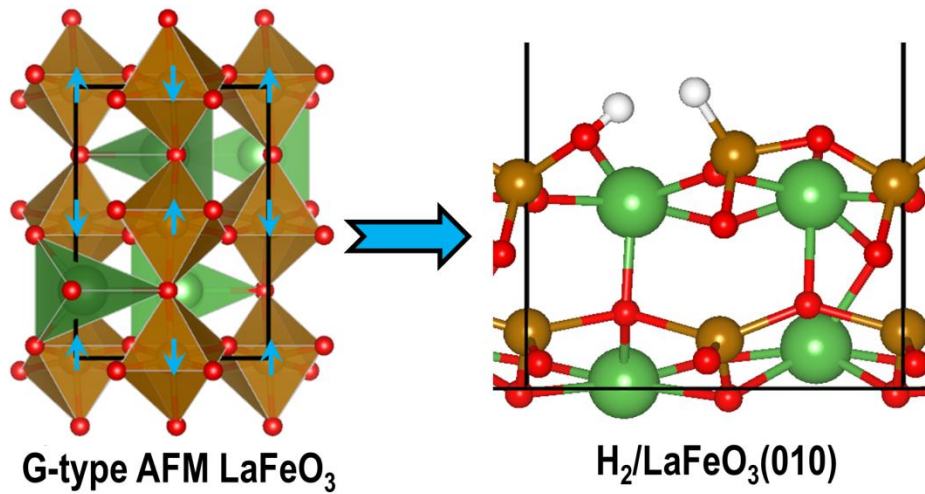
<sup>d</sup> School of Chemistry, Cardiff University, Main Building, Park Place, Cardiff CF10 3AT, UK.

## Abstract

The ABO<sub>3</sub> perovskite lanthanum ferrite (LaFeO<sub>3</sub>) is a technologically important electrode material for nickel-metal hydride batteries, energy storage and catalysis. However, the electrochemical hydrogen adsorption mechanism on LaFeO<sub>3</sub> surfaces remains under debate. In the present study, we have employed spin-polarized density functional theory calculations, with the Hubbard U correction (DFT+U), to unravel the adsorption mechanism of H<sub>2</sub> on the LaFeO<sub>3</sub> (010) surface. We show from our calculated adsorption energies that the preferred site for H<sub>2</sub> adsorption is the Fe-O bridge site, with an adsorption energy of  $-1.178$  eV (including the zero point energy), which resulted in the formation of FeOH and FeH surface species. H<sub>2</sub> adsorption at the surface oxygen resulted in the formation of a water molecule, which leaves the surface to create an oxygen vacancy. The H<sub>2</sub> molecule is found to interact weakly with the Fe and La sites, where it is only physisorbed. The electronic structures of the surface-adsorption systems are discussed *via* projected density of state and Löwdin population analyses. The implications of the calculated adsorption strengths and structures are discussed in terms of the improved design of nickel–metal hydride (Ni–MH) battery prototypes based on LaFeO<sub>3</sub>.

**Keywords:** Lanthanum ferrite (LaFeO<sub>3</sub>), Hydrogen adsorption, Ni-MH batteries, Quantum-ESPRESSO

## Colour Graphic



Lanthanum ferrite (LaFeO<sub>3</sub>) is a technologically important electrode material for nickel-metal hydride batteries, energy storage and catalysis. However, the electrochemical hydrogen adsorption mechanism on LaFeO<sub>3</sub> surfaces remains under debate. In the present study, we have employed spin-polarized density functional theory calculations, with the Hubbard U correction (DFT+U), to unravel the adsorption mechanism of H<sub>2</sub> on the LaFeO<sub>3</sub> (010) surface.

## 1. Introduction

Over the past decade, hydrogen has become increasingly recognised as a promising clean future energy vector. It has both strategic and environmental benefits, since it is carbon- and pollution-free, and has water as its combustion product.<sup>1</sup> Compared to the widely used gasoline and coal, it possesses a higher energy content per unit mass.<sup>2</sup> The key to using hydrogen effectively and safely is the development of novel storage systems, and there is therefore considerable interest in devising novel hydrogen storage media that can store large quantities of hydrogen.<sup>3-10</sup> One of the best solutions is to store it in the solid state in the form of a metal hydride, which is the main material in the negative electrodes of nickel-metal hydride (Ni-MH) secondary batteries,<sup>3, 9, 11</sup> which have a high energy density, good discharge ability at low temperature, long life cycle, no memory effect and are environmentally acceptable.<sup>12-14</sup> Other promising materials that are gaining increased attention for their hydrogen storage potential include carbon nanotubes, metal-doped carbon nanotubes, metal and covalent organic frameworks (MOFs, COFs) and clathrate hydrates.<sup>3-10</sup>

Nanostructured carbon materials, especially carbon nanotubes (CNTs) and carbon nanofibers (CNFs), have received the most attention among emerging materials for hydrogen storage in the solid state, owing to several unique properties.<sup>15-20</sup> For example, in single-walled CNTs, all carbon atoms are exposed at the surface, making this a material with the highest possible surface-to-bulk atom ratio and therefore highly surface active.<sup>15, 18 20</sup> The earliest experiments on the hydrogen storage capacity of CNTs were performed by Dillon and co-workers who obtained 10–20wt% of capacity.<sup>20</sup> Doping CNTs with transition metals that typically form hydrides, including palladium, platinum, and vanadium, is found to increase the hydrogen storage capacity of the CNTs by around 30% without adversely affecting the fast desorption kinetics.<sup>6, 21</sup> For MOFs, the hydrogen sorption behaviour indicates that they reversibly store hydrogen at ambient temperature and moderate pressures, with a typical storage capacity of

1.0wt%,<sup>22-24</sup> which can easily be increased by introducing larger organic moieties into the frameworks.<sup>4</sup>

For portable electrical devices and transport vehicles, such as electric vehicles (EVs), hybrid electric vehicles (HEVs), and plug-in hybrid electric vehicles (PHEVs), rechargeable batteries are regarded as one of the most efficient, simplest, and reliable systems, meeting the criteria established by the U.S. Department of Energy for commercial applications of hydrogen storage systems.<sup>25, 26</sup> To date, most research has focused on developing advanced Li-ion and Ni-MH batteries as high energy density power sources with good environmental compatibility. Ni-MH batteries are considered the preferred choice for practical applications, and are widely studied because of their high capacities, fast charge and discharge capabilities, environmentally friendly characteristics, and long cyclic stability.<sup>27-29</sup> They are also reasonably priced and show a high charge/recharge rate compared to other small-size rechargeable batteries such as Li-ion batteries. Traditional negative electrode materials include AB<sub>5</sub>, AB<sub>2</sub>, AB, and Mg-based alloys.<sup>30-34</sup> Although AB<sub>5</sub>-type alloys have been widely applied in portable electric devices, hand tools and vehicles, they have a high cost and low reversible capacity (about 300 mAh/g). Significant research effort has therefore been expended on the development of new negative electrode materials to reduce the cost and improve the capacity.

In recent years, ABO<sub>3</sub> perovskites have attracted attention as potential negative electrode materials in Ni-MH batteries.<sup>35-41</sup> They are mixed-metal oxides that are of scientific and practical interest because of their low price, adaptability, and thermal stability, which often depends on their bulk and surface characteristics. The perovskite-type oxides ABO<sub>3</sub> have also been widely used in applications such as fuel cells, catalysis, corrosion inhibition and as electrochemical capacitors.<sup>42, 43</sup> Their capacity and stability as anodic materials is much higher than that of traditional materials.<sup>44</sup> The doped perovskite oxide ACe<sub>1-x</sub>M<sub>x</sub>O<sub>3-δ</sub> (d (A = Sr or Ba,

M = rare earth element) was first considered by Esaka *et al.* as an anode material in Ni/MH batteries due to its reasonable hydrogen solubility at room temperature.<sup>36</sup> A  $\text{BaCe}_{0.95}\text{Nd}_{0.05}\text{O}_{3-\delta}$  sample has been demonstrated to store a considerable amount of hydrogen (119 mAh/g) at a discharge current density of 18.5 mA/g. Mandal *et al.* have developed a remarkable intake of hydrogen by  $\text{BaMnO}_3/\text{Pt}$  to the extent of  $\sim 1.25$  mass% at moderate temperatures (190–260 °C) and ambient pressure.<sup>45</sup> The perovskite-type oxide  $\text{LaFeO}_3$  has also been widely considered as a potential negative electrode material in Ni-MH batteries, owing to its high electrochemical capacity and natural abundance.<sup>36, 37, 46</sup> Deng and co-workers showed that the discharge capacity of  $\text{La}_{1-x}\text{Sr}_x\text{FeO}_3$  ( $x = 0.2, 0.4$  and  $0.6$ ) oxide electrodes can reach 543 mAh/g with a current density of 31.25 mA/g at 60 °C, which is much higher than that of  $\text{AB}_5$  alloys.<sup>40</sup> Despite these studies, the electrochemical hydrogen storage mechanism remains unknown, and its elucidation requires molecular-level investigations to understand how the H atoms combine with the perovskite oxide.

In the present study, we have employed spin-polarized DFT calculations with the GGA-PBE exchange-correlation functional to investigate the structures and compositions of the preferred low-index surfaces of  $\text{LaFeO}_3$  and, subsequently, hydrogen adsorption on the (010) surface with the aim to understand the interaction mechanism with the surface and provide theoretical direction for experimental correlation. Understanding the surface adsorption mechanism will enable us to learn to control the pathway of the reactions leading to desired products.

## 2. Computational Details

The calculations were performed within the plane-wave pseudo-potential density functional theory (DFT) method<sup>47, 48</sup> as implemented in the Quantum-ESPRESSO package.<sup>49</sup> Spin-polarized calculations were employed using the generalized gradient approximation (GGA) for the exchange-correlation functional with the Perdew-Burke-Ernzerhof (PBE) functional.

Ultrasoft pseudo-potentials were used, where 5s, 5p, 5d, 6s, and 6p states were considered for La with 11 electrons, 3s, 3p, 3d, 4s, and 4p states for Fe with 16 electrons, 2s and 2p states for O with 6 electrons and the 1s state for H with 1 electron. The Fermi surface effects were treated by the smearing technique of Fermi-Dirac, using a smearing parameter of 0.003 Ry. An energy threshold defining self-consistency of the electron density was set to  $10^{-6}$  eV and a beta defining mixing factor for self-consistency of 0.2. A kinetic-energy cut-off of 30 Ry and charge density cut-off of 180 Ry were used for the smooth part of the electronic wave functions and the augmented electron density, respectively. Brillouin zone integration was done using  $4 \times 4 \times 4$  and  $4 \times 4 \times 1$  Monkhorst-Pack<sup>50</sup> k-point grids (centred at the  $\Gamma$  point) for bulk LaFeO<sub>3</sub> and the surface slab models, respectively. Structural relaxation was carried out to minimize the energy using the conjugate gradient method within the Broyden–Fletcher–Goldfarb–Shanno (BFGS) algorithm,<sup>51</sup> until the magnitude of the residual Hellmann–Feynman force on each relaxed atom reached  $0.01 \text{ eV } \text{\AA}^{-1}$ . Visualization of the structures was obtained using the XCrySDen programme.<sup>52, 53</sup>

We considered the G-type anti-ferromagnetic LaFeO<sub>3</sub> material, which has an orthorhombic perovskite structure, not only in the bulk structure but also in the slab model. The different surface structures were created from the fully optimized bulk structure in order to eliminate the presence of fictitious forces during surface relaxation. To create the surfaces from the bulk, the METADISE code was used,<sup>54</sup> which not only considers periodicity in the plane direction but also provides the different atomic layer stacking resulting in a zero dipole moment perpendicular to the surface plane, as is required for reliable and realistic surface calculations. A vacuum of  $12 \text{ \AA}$  was introduced to the surface models in the z-direction, which is large enough to avoid any spurious interactions between periodic slabs. The relative stabilities of the LaFeO<sub>3</sub> surfaces were determined according to their relaxed surface energy ( $\gamma_r$ ), calculated as:

$$\gamma_r = \frac{E_{slab}^{relaxed} - nE_{bulk}}{2A} \quad (1)$$

where  $E_{slab}^{relaxed}$  is the energy of the relaxed slab,  $nE_{bulk}$  is the energy of an equal number ( $n$ ) of bulk LaFeO<sub>3</sub> atoms,  $A$  is the area of the slab surface and the factor of 2 reflects the fact that there are two surfaces for each slab. Using the calculated surface energies, we have determined the equilibrium crystal morphology of LaFeO<sub>3</sub>, using the Wulff construction approach.<sup>55</sup> According to Wulff's theorem, a polar plot of surface energy versus orientation of normal vectors would give the crystal morphology based on the theory of Gibbs,<sup>56</sup> which showed that under thermodynamic conditions, the equilibrium shape of a crystal should possess minimal total surface free energy for a given volume.

To determine the optimum adsorption sites and geometries for H<sub>2</sub> adsorption, the atoms of the adsorbate and all the atomic layers of the slab were allowed to relax unconstrainedly until residual forces on all atoms had reached 0.01 eV/Å. The reference energy and the bond length of the H<sub>2</sub> molecule in the triplet ground state in the gas-phase were obtained in a cubic cell of size 10 Å. The calculated bond length for H<sub>2</sub>,  $d(\text{H-H})$  is 0.752 Å, which agrees well with the experimental value of 0.74 Å.<sup>57</sup> The nature of the bonding and charge transfer between the H<sub>2</sub> molecule and the interacting surface species were analysed with the projected density of states (PDOS) and a Löwdin population scheme.<sup>58, 59</sup>

### 3. Results and discussion

#### 3.1 Bulk LaFeO<sub>3</sub> Structure

LaFeO<sub>3</sub> occurs in the orthorhombic perovskite structure and belongs to the space group  $Pbnm$ , with four formula units per unit cell as shown in **Figure 1**. The lattice parameters,  $a = 5.6266$  Å,  $b = 5.6083$  Å, and  $c = 7.9401$  Å, reported by Selbach and co-workers,<sup>60</sup> were used as the starting point for our structure optimizations. Full geometry optimization of the lattice

parameters and atomic coordinates was carried out. We have considered different possible magnetic orderings at the  $\text{Fe}^{3+}$  sites in the  $\text{LaFeO}_3$  structure and found that the ground state corresponds to an antiferromagnetic G-type ordering, as shown in **Figure 1**, in agreement with the experimentally reported antiferromagnetic ordering at a Néel temperature of  $T_N = 747 \text{ K}$ .<sup>61</sup> We have also tested different  $U$ -values and their implications for the electronic band-gap and  $\text{Fe}^{3+}$  magnetic moment and found that a value of  $U_{\text{eff}} = 4.64 \text{ eV}$  provides a good description of the band-gap (2.43 eV) and the Fe magnetic moment ( $4.4 \mu_B$ ), which compare well with the experimental band-gap of 2.46 eV<sup>62</sup> and Fe magnetic moment ( $4.6 \pm 0.2 \mu_B$ ).<sup>63</sup> In **Figure 2**, we show how the electronic band-gap increases with increasing strength of the on-site Coulomb repulsion, where  $U = 4.64 \text{ eV}$  predicts the band gap of 2.43 eV, which falls within the experimental range (shaded area). Our predicted  $U_{\text{eff}}$  value compares to the previous theoretical results,<sup>64–66</sup> which showed that  $U_{\text{eff}}$  values in the range of 4.0–4.5 eV provide a good description of the band-gap and magnetic moment of  $\text{Fe}^{3+}$  in  $\text{LaFeO}_3$ . The calculated lattice parameters at  $U_{\text{eff}}$  of 4.64 eV, i.e.  $a = 5.562 \text{ \AA}$ ,  $b = 5.673 \text{ \AA}$ , and  $c = 7.934 \text{ \AA}$ , are also in good agreement with experimental data.<sup>67</sup> In addition to the lattice parameters, the calculated Fe–O–Fe bond angles (axial and equatorial) and the weak Fe–O (axial and equatorial) bond lengths reproduce the experimental data (**Table 1**).

**Table 1** shows a comparison between the structural, electronic, and magnetic properties for antiferromagnetic  $\text{LaFeO}_3$  calculated with GGA and GGA+U functionals. We found that although both the pure GGA and GGA+U predict a band gap for  $\text{LaFeO}_3$ , pure GGA significantly underestimates the band gap (1.00 eV in this study, and 0.75 eV in Ref.<sup>65</sup>) and the Fe magnetic moments ( $4.1 \mu_B$  in this study and  $3.7 \mu_B$  in Ref.<sup>65</sup>). These errors may arise from the self-interaction inherent in pure density functionals for strongly correlated systems that can be improved by the DFT+U approach, which accounts for the on-site Coulomb interaction in

the relevant d orbitals. This effect is seen from the more accurate values for the band gap and magnetic moments obtained by the GGA+U calculations, listed in **Table 1**.

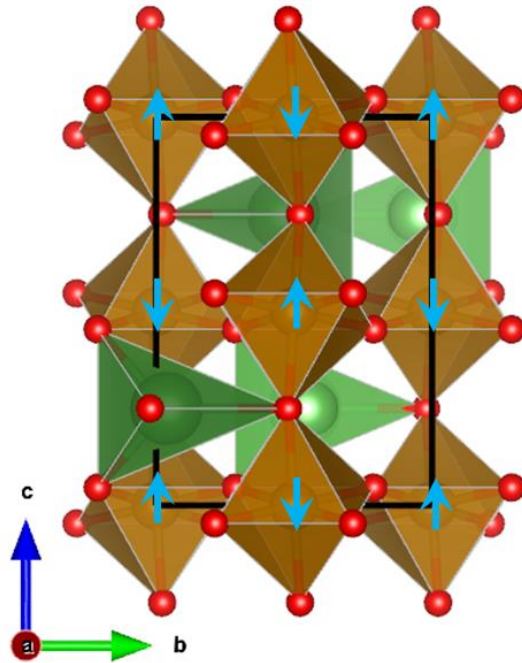


**Figure 1:** Structure of LaFeO<sub>3</sub> in terms of FeO<sub>6</sub> and LaO<sub>4</sub> octahedra with the G-type AFM spin ordering indicated by up and down arrows at the Fe sites.

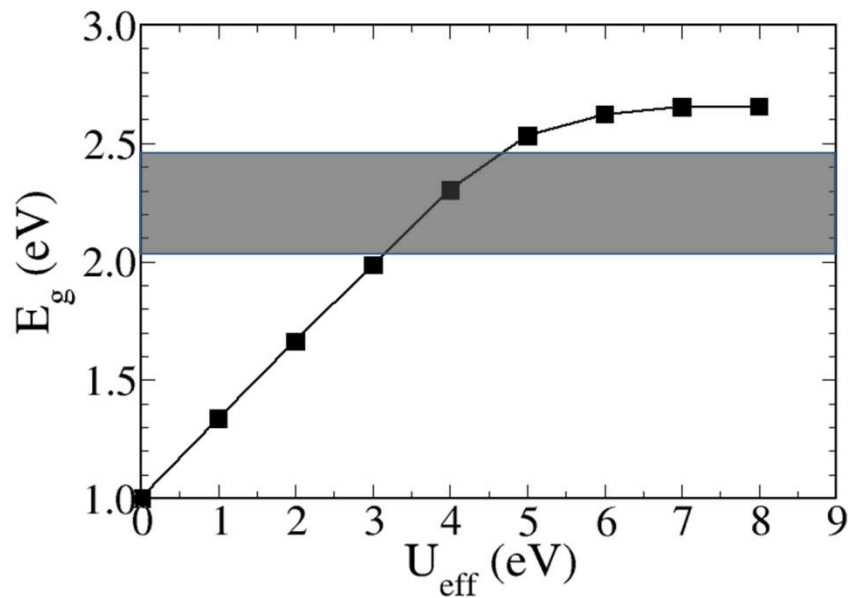


**Figure 2** Electronic band gap,  $E_g$  for LaFeO<sub>3</sub> plotted against different  $U_{\text{eff}}$  values. The experimental band-gap range is indicated by the shaded area.

**Table 1:** Calculated and experimental lattice constants ( $a$ ,  $b$ ,  $c$ ), axial and equatorial Fe–O bond lengths ( $r_z$  and  $r_{xy}$ , respectively), axial and equatorial Fe–O–Fe bond angles ( $\alpha_z$  and  $\alpha_{xy}$ , respectively), eigenvalue gap ( $E_g$ ), Fe magnetic moment ( $\mu_{\text{Fe}}$ ) and cell volume ( $V$ ) for orthorhombic LaFeO<sub>3</sub>.

Property	This work			Literature		
	GGA	GGA+U U =4.3eV	GGA+U U =4.64 eV	Expt.	GGA	GGA+U U =4.3eV
$a$ (Å)	5.529	5.565	5.562	5.553 <sup>a</sup>	5.556 <sup>b</sup>	5.572 <sup>b</sup>
$b$ (Å)	5.638	5.664	5.673	5.563 <sup>a</sup>	5.653 <sup>b</sup>	5.627 <sup>b</sup>
$c$ (Å)	7.879	7.934	7.934	7.862 <sup>a</sup>	7.885 <sup>b</sup>	7.901 <sup>b</sup>
$r_z$ (Å)	2.033	2.054	2.033	2.009 <sup>a</sup>	2.025 <sup>b</sup>	2.028 <sup>b</sup>
$r_{xy}$ (Å)	2.035	2.046	2.044	2.007 <sup>a</sup>	2.046 <sup>b</sup>	2.035 <sup>b</sup>
$\alpha_z$ (°)	151.20	149.97	151.30	156.32 <sup>a</sup>	153.54 <sup>b</sup>	153.80 <sup>b</sup>
$\alpha_{xy}$ (°)	152.06	151.36	152.54	157.22 <sup>a</sup>	153.72 <sup>b</sup>	154.69 <sup>b</sup>
$E_g$ (eV)	1.00	2.38	2.43	2.46 <sup>d</sup>	0.75 <sup>b</sup>	2.53 <sup>b</sup>
$\mu_{\text{Fe}}$ ( $\mu_B$ )	4.1	4.3	4.4	4.6±0.2 <sup>c</sup>	3.7 <sup>b</sup>	4.2 <sup>b</sup>
$V$ (Å <sup>3</sup> )	245.583	250.073	250.340	242.868 <sup>a</sup>	247.653 <sup>b</sup>	247.730 <sup>b</sup>

<sup>a</sup> Reference 67; <sup>b</sup> Reference 65; <sup>c</sup> Reference 63; <sup>d</sup> Reference 63

### 3.2 Surface model

Prior to studying hydrogen adsorption and consequent surface reactions, we have characterized the structures and relative stabilities of the (010), (110), and (111) surfaces, which are the commonly observed surface planes in  $ABO_3$  perovskites such as  $LaFeO_3$ ,  $BaTiO_3$ ,  $SrTiO_3$ ,  $LaAlO_3$  and  $BaZrO_3$ .<sup>68–74</sup> Shown in **Figure 3** are the optimized structures of the clean surfaces of  $LaFeO_3$ . The surface energies of the (110), (111), and (010) surfaces are calculated at 0.88, 0.94, and  $1.02 \text{ J m}^{-2}$  respectively, suggesting that the order of decreasing stability of the  $LaFeO_3$  surfaces is  $(110) < (111) < (010)$ . The resulting equilibrium morphology (Wulff shape) of a single crystal of  $LaFeO_3$ , obtained from the calculated surface energies, is shown in **Figure 4**, with all three facets distinctly expressed in the equilibrium morphology.

After geometry optimization of the  $LaFeO_3$  surfaces, where all atomic positions were allowed to relax unconstrainedly, no reconstruction was observed, in accord with the predictions of Liu and co-workers.<sup>75</sup> Due to the change in the coordination of the topmost surface ions compared to the bulk, we found that the  $LaFeO_3$  (010), (110), and (111) surfaces exhibit large relaxations in its interlayer spacings ( $\Delta d_{ij}$ ), reported in **Table 2**. The percentage relaxation of the interlayer spacings of the (010) surface was calculated using the relation:

$$\Delta d_{ij} = \frac{(d_{ij} - d_{bulk})}{d_{bulk}} \times 100 \quad (2)$$

where negative values correspond to inward relaxation (contraction), with positive values denoting outward relaxation (dilation) of the interlayer spacings. The interlayer relaxations can be understood by considering the fact that when a crystal is cut to form a surface, the electrons rearrange in order to reduce the charge-density corrugations and thus their kinetic energy according to the Smoluchowski model.<sup>76</sup> This leads to a motion downwards into the crystal of the electrons left on top of the surface atoms, resulting in an electrostatic attraction of the top

layer ions to the rest of the crystal. As the redistribution of the electronic density extends over several layers, it gives rise to a damped oscillatory nature of the relaxation, *i.e.*, alternating contractions and dilatations.<sup>77</sup> The topmost three percentage interlayer spacing relaxations ( $\Delta d_{12}$ ,  $\Delta d_{23}$ ,  $\Delta d_{34}$ ) of the  $\text{LaFeO}_3$  (010), (111), and (110) surfaces are calculated at  $-43.3$ ,  $+16.6$ , and  $-58.3$  %;  $-31.9$ ,  $+13.6$  and  $-21.5$  %; and  $-32.7$ ,  $+10.4$  and  $+27.2$  %, respectively. The contractions in the first to second layer ( $\Delta d_{12}$ ) spacings can be attributed to the downward movement of the terminating O ions towards the bulk during geometry optimization.

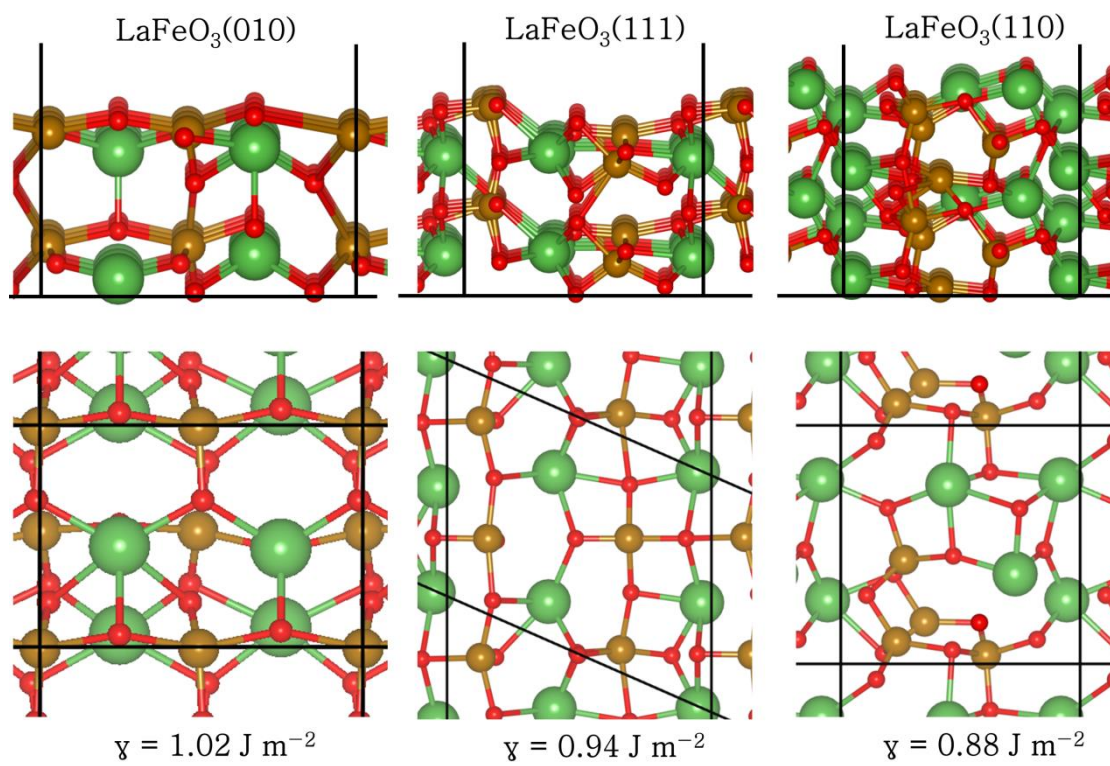


**Figure 3:** The optimized structures of the (010), (111) and (110) surfaces of  $\text{LaFeO}_3$  in side (top) and top (bottom) views.

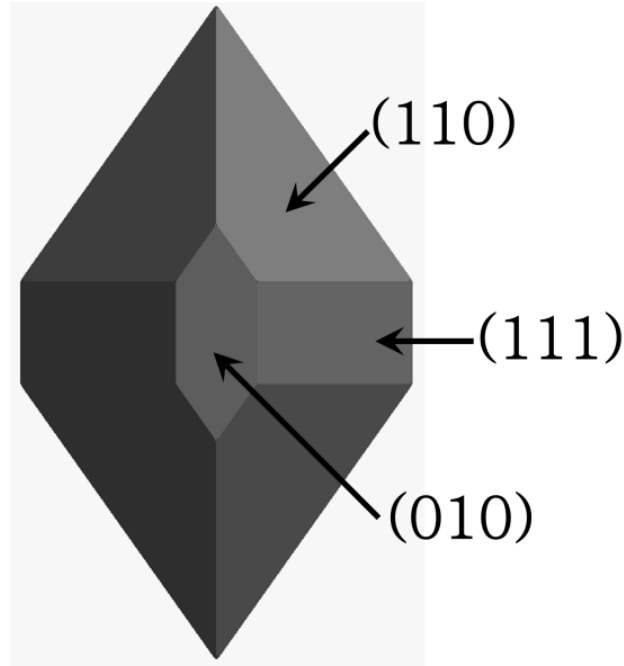


**Figure 4:** Wulff construction of the equilibrium crystal morphology of LaFeO<sub>3</sub>.

**Table 2:** Surface relaxation of the unreconstructed clean surface of LaFeO<sub>3</sub>

$d_{ij}$ /surface	Interlayer spacing Relaxation (%)		
	(010)	(111)	(110)
$d_{12}$	-43.28	-31.92	-32.65
$d_{23}$	+16.62	+13.59	+10.39
$d_{34}$	-58.34	-21.54	-27.16
$d_{45}$	+57.14	+19.53	+20.82

### 3.3 Hydrogen adsorption

Following the trend generally observed for surface reactivity, where the thermodynamically less stable surfaces are more reactive towards adsorbing species,<sup>78–80</sup> the LaFeO<sub>3</sub> (010) surface was chosen to investigate hydrogen adsorption and its surface-bound reactions, as the (010) is the least stable among the three surfaces studied, but is still a significant surface

in the equilibrium morphology. The (010) plane is also the most examined surface of ABO perovskites such LaFeO<sub>3</sub>, BaTiO<sub>3</sub>, SrTiO<sub>3</sub>, LaAlO<sub>3</sub> and BaZrO<sub>3</sub>.<sup>68-74</sup>

Different high symmetry adsorption sites, *i.e.* on top of the Fe, La, or O sites or their bridging sites, as presented in **Figure 4**, were examined in order to characterise the adsorption strength and properties of hydrogen molecules on the LaFeO<sub>3</sub> (010) surface. However, after initially placing the adsorbates above these sites, they were free to move away from the sites during geometry optimization, thus ensuring that as far as possible the lowest-energy surface-adsorbate structures were obtained. Three distinct adsorption states were investigated for the adsorbed H<sub>2</sub>, with H-H bonds at molecular (0.74 Å), dihydrogen (~ 0.80 Å) and dihydride (~ 1.70 Å) distances.<sup>81</sup> The molecular, dihydrogen, and dihydride states are denoted as M, DHG, and DHD in the manuscript. For the molecular and dihydrogen adsorption states, we have placed the H<sub>2</sub> molecule on the surface in either a head-on configuration, with the H<sub>2</sub> adsorbed vertically pointing towards the surface, or a side-on configuration, where the H<sub>2</sub> is adsorbed parallel to the surface plane at top or bridge sites.

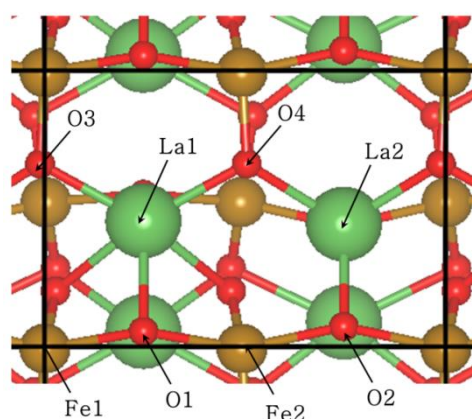


**Figure 4:** High symmetry adsorption sites on the LaFeO<sub>3</sub> (010) surface. (Colour code: Fe = silver, La = green, and O =red).

To evaluate the strength of the interaction between H<sub>2</sub> and the different adsorption sites on the LaFeO<sub>3</sub> (010) surface, we have calculated the adsorption energies ( $E_{\text{ads}}$ ) defined as follows:

$$E_{ads} = E_{surface+H_2} - (E_{surface} + E_{H_2}) \quad (3)$$

where  $E_{surface+H_2}$  is the total energy of the substrate-adsorbate system in the equilibrium state,  $E_{surface}$  and  $E_{H_2}$  are the total energies of the substrate (clean surface) and adsorbate (free molecule), respectively. By this definition, a negative value  $E_{ads}$ , corresponds to an exothermic and favourable adsorption process, whereas a positive value indicates an endothermic and unfavourable adsorption process. Also, the larger the  $E_{ads}$ , the more stable is the structure of the slab+H<sub>2</sub>. The distortion energy ( $E_{dist}$ ) which represents the energy of the distortion of the geometry of the free adsorbate after adsorption on the surface is also calculated as follows:

$$E_{dist} = E_{distorted-molecule} - E_{free-molecule} \quad (4)$$

where  $E_{free-molecule}$  is the energy of free molecule in the gas phase, whereas  $E_{distorted-molecule}$  is the energy of the isolated molecule, but retaining the distorted geometry as found in its adsorbed state on the surface. To calculate  $E_{distorted-molecule}$  we first optimized the H<sub>2</sub>/LaFeO<sub>3</sub>(010) complex, then removed the surface and performed a single point calculation of the H<sub>2</sub> molecule in its adsorbed geometry as found in the optimized H<sub>2</sub>/LaFeO<sub>3</sub>(010) complex.. In this work, all of the reported energies were corrected by the zero-point energy ( $\Delta ZPE$ ), calculated as the difference between the ZPE of the H<sub>2</sub> molecule on the surface and in the gas phase according to Equation 5:

$$\Delta ZPE = \left( \sum_{i=1}^{3n} \frac{h\nu_i}{2} \right)_{surf} - \left( \sum_{i=1}^{3n} \frac{h\nu_i}{2} \right)_{gas} \quad (5)$$

where  $h$  is Planck constant and  $\nu_i$  are the vibrational frequencies.

The configurations of the initial and final adsorption structures of H<sub>2</sub> at selected sites where product(s) were formed upon hydrogen adsorption are shown in **Figure 5**, whereas the adsorption and distortion energies and relevant bond distances are summarized in **Tables 3** and

4. The adsorption structures are labelled in relation to the adsorption site numbers in **Figure 4**. The lowest-energy structures for H<sub>2</sub> adsorbed in molecular, dihydrogen and dihydride states were calculated at the Fe2 and O2 sites (**Figure 5d**). Each initial adsorption state yields the same product (La-OH and Fe-H), thus releasing the same adsorption energy of 1.323 eV (*i.e.* 1.178 eV including the ZPE correction) as the reference hydrogen molecule is the same. The distortion energy of hydrogen to form the product (La-OH and Fe-H) was calculated at 0.116 meV. The strong interaction of the hydrogen molecule with the Fe2 and O2 sites resulted in significant relaxation of the topmost surface species, with the interacting Fe2 and O2 species moving downwards and upwards by 0.38 and 0.25 Å, respectively, in the direction perpendicular to the surface from their initial surface positions, while the unbound Fe and O species sink into the surface by 0.99 and 0.35 Å, respectively. Similar adsorption structures were calculated for H<sub>2</sub> adsorbed at either Fe1-O1 or Fe2-O1 bridge sites, in molecular, dihydrogen and dihydride states, which released a common adsorption energy of 0.46 eV (*i.e.* 0.39 eV including the ZPE correction). The distortion energy of hydrogen molecule at the Fe1-O1 or Fe2-O1 bridge sites was calculated to be ~0.207 meV. Compared to the Fe2-O2 bridge site adsorption (**Figure 5c**), the weaker interactions of H<sub>2</sub> at either Fe1-O1 or Fe2-O1 bridge sites resulted in minimal relaxations of the surfaces species. The interacting Fe and O atoms were pulled upwards by 0.39 and 0.41 Å, respectively, in the direction perpendicular to the surface from their initial surface positions, while the unbound Fe and O species sink into the surface by 0.20 and 0.25 Å, respectively.

Weaker interactions were calculated when H<sub>2</sub> is adsorbed in the molecular and dihydrogen states at the oxygen sites, compared with adsorption as a dihydride (**Table 3**). The adsorption of H<sub>2</sub> at molecular, dihydrogen and dihydride H–H bond distances at the O1 site results in the formation of a H<sub>2</sub>O molecule which leaves the surface, thereby creating an oxygen vacancy, which may be an efficient active site for catalytic activity on the LaFeO<sub>3</sub> (010) surface. The

H–O–H bond angle of the formed H<sub>2</sub>O molecule was calculated at 105.72 ° which is similar to that of a gas phase H<sub>2</sub>O molecule (104.5 °). The creation of the O vacancy due to the dihydride adsorption results in significant structural changes of the (010) surface, with existing bonds breaking and new ones being formed. We have also observed significant inward relaxation of the topmost Fe ions and outward relaxations of the La ions. The Fe and La ions move downward by 0.51 and 0.04 Å, respectively, in the direction perpendicular to the surface from their initial surface positions. The formation of H<sub>2</sub>O was also observed at the O2 and O4 sites. However, out of the three O sites (O1, O2 and O4), it is only the O4 site that promotes H<sub>2</sub>O removal from the surface with an associated vacancy-hopping oxygen transport mechanism, where another O atom within the surface structure attempts to fill the created vacancy. The adsorption of H<sub>2</sub> in head-on configurations gave very weak adsorption energies (0.01–0.06 eV), as the molecule was only physisorbed and did not dissociate to form adsorbate species (products) at the various adsorption sites investigated. The adsorption energies calculated for the H<sub>2</sub> adsorbed at molecular, dihydrogen and dihydride H–H distances are summarized in **Table 4**. Due to the very weak interactions with the surface of the H<sub>2</sub> molecule when adsorbed head-on on the (010) surface, no significant changes were observed in the surface structure.

According to Atkins and co-workers,<sup>82</sup> for LaFeO<sub>3</sub> to be used as an anodic material in Ni-MH batteries, the ideal adsorption energy (bond enthalpy) should be in the range of 0.26–0.52 eV. If the adsorption energy is too high, the overall reaction in the Ni-MH battery will not be reversible. The M (LaFeO<sub>3</sub> in this study) is supposed to possess a high hydrogen adsorption capacity and moderate hydride stability in Ni-MH battery applications. Hence, the Fe2-O1 bridge site was chosen as the most favourable site, as the adsorption energy released at this site is approximately 0.40 eV with ZPE correction. At the Fe2-O1 bridge site, the Fe coordinates to three O atoms and two La atoms at an average Fe–O bond length of 1.998 Å, an average

La–Fe bond length of 3.248 Å and an O–Fe–O bond angle of 90.22°. The O atom also coordinates to two Fe atoms at an average Fe–O bond length of 2.081 Å with an Fe–O–Fe bond angle of 148.73°.

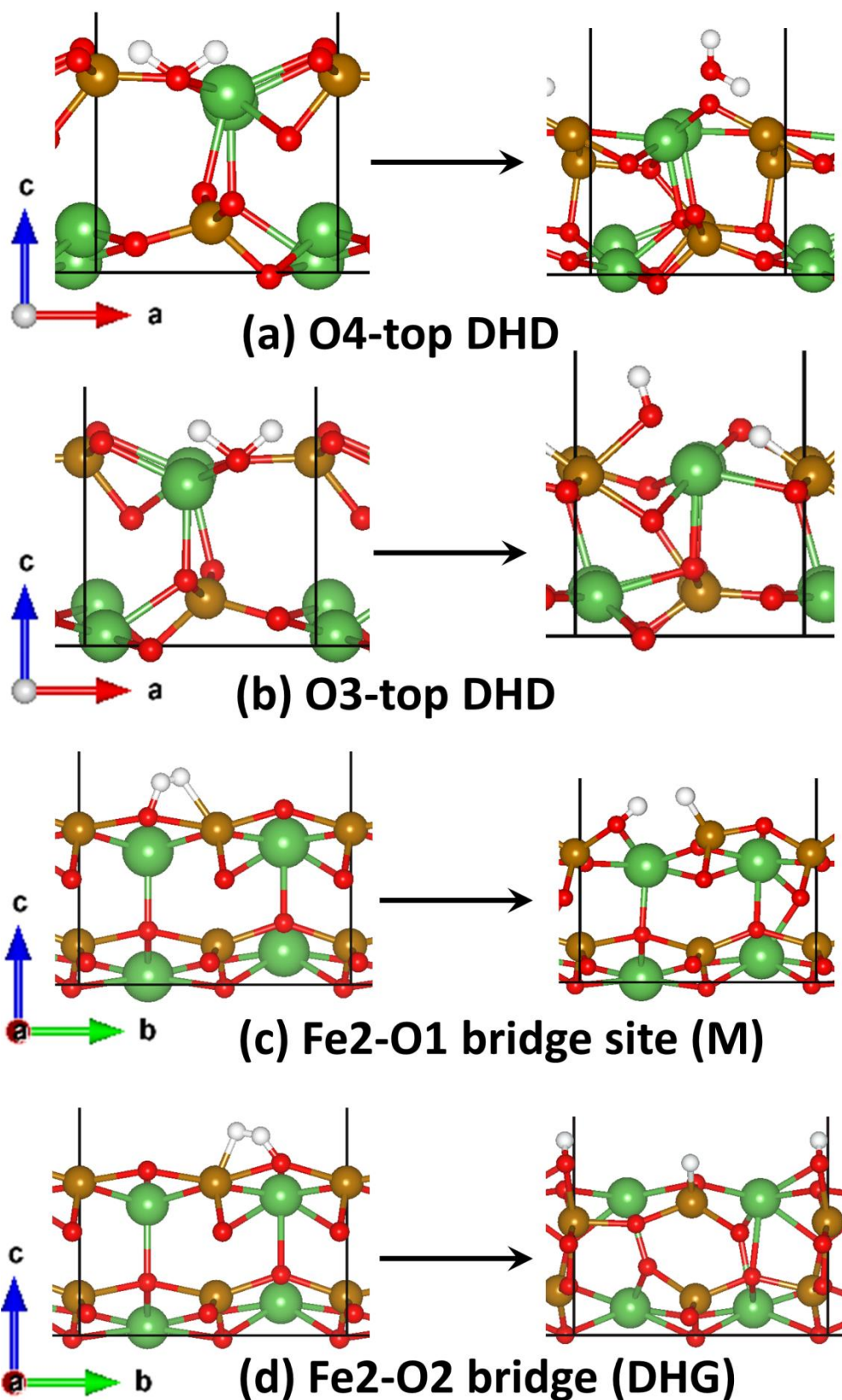


**Figure 5:** Side views of the initial and optimized geometries of all the different kind of adsorbate species that form at selected favourable adsorption sites. (Colour code: Fe = silver, La = green, O = red, and H = white).

**Table 3:** Calculated adsorption energy ( $E_{\text{ads}}$ ) and the adsorbate species formed (products) at the favourable adsorption sites. The  $E_{\text{ads}}$  corrected by the ZPE is shown in parentheses.

Adsorption site	Molecular		Dihydrogen		Dihydride	
	$E_{\text{ads}}$ /eV	Product(s)	$E_{\text{ads}}$ /eV	Product(s)	$E_{\text{ads}}$ /eV	Product(s)
O1-top side-on	-0.218 (-0.157)	H <sub>2</sub> O	-0.174 (-0.105)	H <sub>2</sub> O	-0.331 (-0.251)	H <sub>2</sub> O
O2-top side-on	-0.053 (+0.007)	---	-0.056 (+0.024)	---	-0.612 (-0.502)	H <sub>2</sub> O
O3-top side-on	-0.235 (-0.165)	LaOH and FeH	-0.238 (-0.134)	LaOH and FeH	-0.487 (-0.394)	FeOH and FeH
O4-top side-on	-0.232 (-0.160)	LaOH and FeH	-0.236 (-0.140)	LaOH and FeH	-0.509 (-0.428)	H <sub>2</sub> O
Fe1-O1 bridge	-0.455 (-0.392)	Fe( $\mu$ OH)La and FeH	-0.455 (-0.393)	Fe( $\mu$ OH)La and FeH	-0.455 (-0.397)	Fe( $\mu$ OH)La and FeH
Fe2-O1 bridge	-0.456 (-0.391)	Fe( $\mu$ OH)La and FeH	-0.456 (-0.392)	Fe( $\mu$ OH)La and FeH	-0.455 (-0.392)	Fe( $\mu$ OH)La and FeH
Fe2-O2 bridge	-1.323 (-1.178)	FeOH and FeH	-1.322 (-1.172)	LaOH and FeH	-1.324 (-1.176)	LaOH and FeH
La1-O1 bridge	-0.039 (+0.011)	---	-0.039 (+0.018)	---	-0.457 (-0.393)	Fe( $\mu$ OH)La and FeH
La1-Fe1 bridge	-0.028 (+0.032)	---	-0.025 (+0.012)	---	-0.697 (-0.597)	Fe( $\mu$ OH)La and FeH

**Table 4:** Calculated adsorption energy ( $E_{\text{ads}}$ ) at the other adsorption sites which gave no product(s)

Adsorption site	Molecular	Dihydrogen	Dihydride
	$E_{\text{ads}} / \text{eV}$	$E_{\text{ads}} / \text{eV}$	$E_{\text{ads}} / \text{eV}$
O4-top head-on	-0.026	-0.028	-0.024
O3-top head-on	-0.026	-0.027	-0.026
O1-top head-on	-0.030	-0.030	-0.030
O2-top head-on	-0.034	-0.031	-0.033
Fe2-top head-on	-0.012	-0.011	-0.027
Fe2-top head-on	-0.012	-0.011	-0.015
Fe1-top head-on	-0.012	-0.012	-0.029
Fe1-top head-on	-0.015	-0.011	-0.015
La2-top head-on	-0.059	-0.059	-0.062
La2-top head-on	-0.012	-0.012	-0.062
La1-top head-on	-0.039	-0.039	-0.046
La1-top head-on	-0.046	-0.047	-0.045
La2-O2 bridge	-0.034	-0.034	-0.046
La2-O2 bridge	-0.055	-0.051	-0.052
La2-Fe2 bridge	-0.026	-0.023	0.018
La1-O4 bridge	-0.030	-0.031	-0.038
La1-O3 bridge	-0.029	-0.029	-0.037
La1-Fe2 bridge	-0.032	-0.031	-0.021
La1-La2 bridge	-0.029	-0.030	-0.026

### 3.4 Electronic Structures

In order to evaluate the effect of hydrogen adsorption on the electronic structure of the  $\text{LaFeO}_3$  (010) surface, we have determined and analysed the density of states (DOS) projected on the hydrogen, oxygen and iron atoms in the first surface layer of the  $\text{LaFeO}_3$  (010) surface, before and after adsorption, for the most stable adsorption site (Fe2-O1 bridge) (shown in **Figure 6 and 7**). By analysing the changes in valence states and energies, information is obtained on the

interactions between the atoms. Before adsorption, the H<sub>2</sub> molecule exhibits sharp peaks at around -6 eV and 5 eV, respectively. After adsorption and dissociation into H atoms, the s-orbital peaks shift to lower energies, which is consistent with stabilization of the hydrogen molecule. The peak heights are lowered and new peaks appear, which indicates strong interactions between the hydrogen and the interacting surface species. Due to the interaction of the hydrogen molecule, we have also observed changes in the projected DOS on the interacting surface O and Fe atoms. These changes are found to affect the Fe magnetic moments, as they increase from 4.550 μ<sub>B</sub> to 4.605 μ<sub>B</sub> after the adsorption of hydrogen. Further insight into the nature of the interactions of the hydrogen molecule with the LaFeO<sub>3</sub> (010) surface was obtained through Löwdin charge population analyses. Population analysis is a tool widely used by chemists to rationalize molecular properties by determining the distribution of electrons in a molecule among each of its constituent atoms. The Löwdin charge population analysis was computed using the technique described by Sanchez-Portal and co-workers.<sup>83</sup> The Löwdin charges of the configuration of the most stable hydrogen adsorption site (Fe2-O1 bridge), before and after H<sub>2</sub> adsorption, are listed in **Table 8**. The molecular, dihydrogen, and dihydride H<sub>2</sub> gained charges of -0.17 e<sup>-</sup>, -0.18 e<sup>-</sup> and -0.24 e<sup>-</sup>, respectively, from the LaFeO<sub>3</sub> (010) surface, mainly from the interacting surface species. The charge gained by the hydrogen caused the molecular and dihydrogen H-H bonds, which were initially at 0.740 Å and 0.796 Å, respectively, to break after adsorption, increasing the H-H distance to 1.634 Å. The Fe atom which interacts with the adsorbing H<sub>2</sub> atom, loses a charge of 0.21 e<sup>-</sup>, whether H<sub>2</sub> adsorbs as molecular, dihydrogen or dihydride species, suggestive of further oxidation of the Fe<sup>3+</sup> ions. Similar observations were made by Hoffmann and co-workers who reported a change of valence states of the B site in perovskite ABO<sub>3</sub> structure.<sup>84</sup>

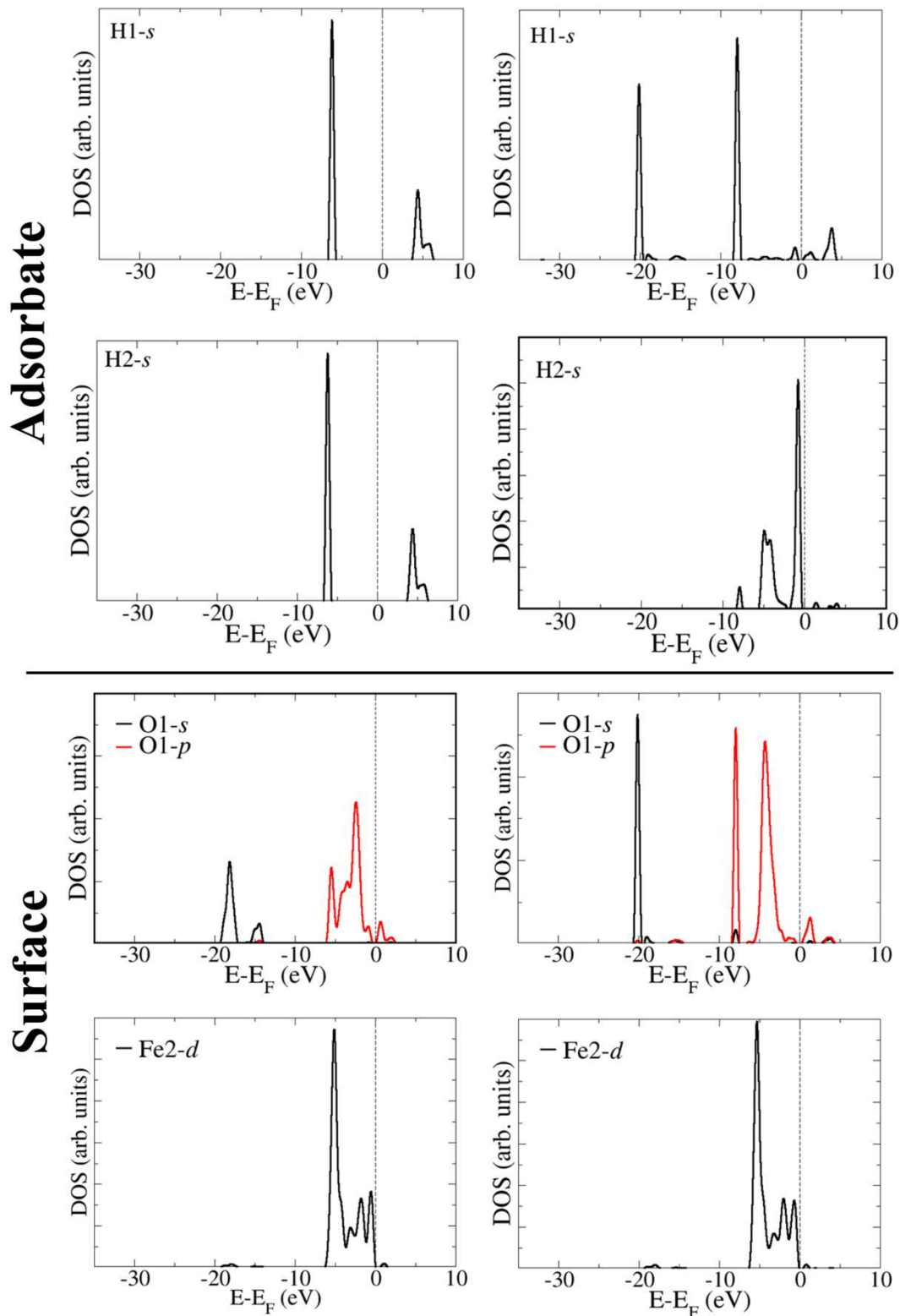


**Figure 6:** Top panel: PDOS for H<sub>2</sub> molecule before (left) and after (right) adsorption on the most stable Fe2-O1 bridge site at molecular hydrogen bond distance. Down panel: PDOS for the interacting iron (Fe2) and oxygen (O1) before (left) and after (right) the adsorption of hydrogen at molecular bond distance Fe2-O1 bridge site.

**Table 8** Löwdin Charge Population results for LaFeO<sub>3</sub> (0 1 0) surface before and after H<sub>2</sub> adsorption: Fe2-O1 bridge site.

Atom	Molecular			Dihydrogen			Dihydride		
	Q <sub>before</sub> (e <sup>-</sup> )	Q <sub>after</sub> (e <sup>-</sup> )	ΔQ (e <sup>-</sup> )	Q <sub>before</sub> (e <sup>-</sup> )	Q <sub>after</sub> (e <sup>-</sup> )	ΔQ (e <sup>-</sup> )	Q <sub>before</sub> (e <sup>-</sup> )	Q <sub>after</sub> (e <sup>-</sup> )	ΔQ (e <sup>-</sup> )
H1	0.038	0.384	-0.346	0.034	0.384	-0.350	0.004	0.384	-0.380
H2	0.038	-0.140	0.178	0.034	-0.140	0.173	0.004	-0.138	0.142
Fe1	0.664	0.454	0.210	0.664	0.454	0.210	0.664	0.451	0.213
Fe2	0.664	0.628	0.036	0.664	0.628	0.036	0.664	0.627	0.037
La1	0.953	0.986	-0.034	0.953	0.986	-0.034	0.953	0.987	-0.035
La2	0.957	0.980	-0.022	0.957	0.980	-0.022	0.957	0.977	-0.020
O1	-0.527	-0.581	0.054	-0.527	-0.581	0.054	-0.527	-0.581	0.055
O2	-0.533	-0.473	-0.060	-0.533	-0.473	-0.060	-0.533	-0.472	-0.061
O3	-0.524	-0.539	0.014	-0.524	-0.539	0.014	-0.524	-0.538	0.013
O4	-0.524	-0.523	-0.002	-0.524	-0.523	-0.002	-0.524	-0.523	-0.002

#### 4. Summary and Conclusions

We have used spin-polarized density functional theory calculations with Hubbard U correction (DFT+U) to calculate the bulk structures and electronic properties of bulk LaFeO<sub>3</sub>. In order to assess the use of LaFeO<sub>3</sub> as an anodic material in Ni-MH batteries, we have also investigated the adsorption of hydrogen gas on the LaFeO<sub>3</sub> (010) surface. The GGA+U implementation provides the best model for describing bulk LaFeO<sub>3</sub>, which is calculated to be a G-type antiferromagnetic insulating material with a band gap of 2.43 eV and a Fe magnetic moment of 4.4  $\mu_B$ , in close agreement with experimental data. The strong adsorption energy of -1.18 eV released from the formation of FeOH and FeH, when the hydrogen molecule is adsorbed at the Fe2-O2 bridge site, suggests a relatively high hydrogen storage capacity of LaFeO<sub>3</sub>. On the other hand, the lower adsorption energies of -0.40 eV released from the Fe1-O1 and Fe2-O1 bridge sites suggest that these sites offer easy release of the adsorbed hydrogen atoms for electrochemical reactions. This energy also falls within the ideal adsorption energy (bond enthalpy) range of 0.26–0.52 eV for materials to be used as anodic materials in Ni-MH batteries, according to Atkins and co-workers.<sup>82</sup> We have observed water formation at the O-top site, irrespective of the form in which the H<sub>2</sub> is adsorbed, which creates an oxygen vacancy at the surface. The adsorption of hydrogen on the LaFeO<sub>3</sub> (010) surface is shown to be characterized by hybridization of the H-1s states and the interacting surface O-2p states and Fe-3d states, which results in a small charge transfer from the surface to the adsorbing hydrogen molecule. The calculated low adsorption energies of hydrogen at the LaFeO<sub>3</sub> (010) surface have implications for the use of LaFeO<sub>3</sub> in Ni-MH battery applications. The adsorbed hydrogen atoms can be released/desorbed at practical temperatures and pressures at the LaFeO<sub>3</sub> (010) surface, compared to other AB<sub>2</sub> Zr-based alloys which have poor hydrogen desorption characteristics.<sup>85, 86</sup> The molecular-level information provided in the present study provides fundamental insight into the adsorption mechanism of hydrogen on the LaFeO<sub>3</sub> (010) surface

and should be useful in the design of nickel–metal hydride (Ni–MH) battery prototypes based on the  $ABO_3$  perovskite  $LaFeO_3$ .

### Acknowledgements

The authors gratefully acknowledge the UK's Royal Society and the Leverhulme Trust for a research grant under the Royal Society-Leverhulme Africa Award Scheme. EA, RT and IWB acknowledge the National Council for Tertiary Education, Ghana, for a TALIF research grant.

### References

1. H. Balat and E. Kirtay, *Inter. J. Hydro. Energy*, 2010, **35**, 7416–7426
2. I. K. Kapdan and F. Kargi, *Enzym Micro Tech.*, 2006, **38**, 569–582.
3. A. Züttel, *Materials Today*, 2003, **6**, 24–33.
4. N. L. Rosi, J. Eckert, M. Eddaoudi, M. Eddaoudi, D. T. Vodak, J. Kim, M. O'Keeffe and O. M. Yaghi, *Science*, 2003, **300**, 1127–1129.
5. E. Klontzas, E. Tylianakis and G. E. Froudakis, *J. Phys. Chem. C*, 2008, **112**, 9095–9098.
6. R. Zacharia, S.-U. Rather, S. W. Hwang and K. S. Nahm, *Chem. Phys. Lett.*, 2007, **434**, 286–291.
7. J. Weitkamp, M. Fritz and S. Ernst, *Int. J. Hydrogen Energy* 1995, **20**, 967–970.
8. H. Lee, J.-W. Lee, D. Y. Kim, J. Park, Y.-T. Seo, H. Zeng, I. L. Moudrakovski, C. I. Ratcliffe and J. A. Ripmeester, *Nature*, 2005, **434**, 743–746.
9. H. Reardon, J. M. Hanlon, R. W. Hughes, A. Godula-Jopek, T. K. Mandal and D. H. Gregory, *Energy Environ. Sci.* 2012, **5**, 5951–5979.
10. S. S. Han, H. Furukawa, O. M. Yaghi and I. W. A. Goddard, *J. Am. Chem. Soc.*, 2008, **130**, 11580–11581
11. Q. R. Yao, H. Y. Zhou, Z. M. Wang, S. K. Pan and G. H. Rao. *J. Alloys Comp* 2014, **606**, 81–85.
12. C. B Jung and K. S. Lee, *J Alloys Comp* 1997, **253–254**, 605–608.
13. T. Kohno, M. Yamamoto and M. Kanda. *J Alloys Comp* 1999, **293–295**, 643–647.
14. T. Sakai, H. Miyamura, N. Kuriyama, A. Kato, K. Oguro and H. Ishikawa, *J Electrochem Soc* 1990, **137**, 795–799.

15. Y. Ye, C. C. Ahn, C. Witham and B. Fultz, *Appl. Phys. Lett.* 1999, **74**, 2307–2309.
16. K. Shindo, T. Kondo, and Y. Sakurai, *J Alloys Comp*, 2004, **379**, 252–255.
17. K. A. Williams and P. C. Eklund, *Chem. Phys. Lett.* 2000, **320**, 352–358.
18. N. Rajalakshmi, K. S. Dhathathreyan, A. Govindaraj and B. C. Satishkumar, *Electrochim. Acta*, 2000, **45**, 4511–4515.
19. C. Nützenadel, A. Züttel, D. Chartouni and L. Schlapbach, *Electrochem Solid-State Lett*, 1999, **2**, 30–32.
20. A. C. Dillon, K. M. Jones, T. A. Bekkedahl, C. H. Kiang, D. S. Bethune and M. J. Heben, *Nature*, 1997, **386**, 377–379.
21. R. Zacharia, K. Y. Kim, A. K. M. Fazle Kibria and K. S. Nahm, *Chem. Phys. Lett.*, 2005, **412**, 369–375.
22. H. W. Langmi, J. Ren, B. North, M. Mathe and D. Bessarabov, *Electrochim. Acta*, 2014, **128**, 368–392.
23. L. J. Murray, M. Dinc and J. R. Long, *Chem. Soc. Rev.* 2009, **38**, 1294–1314.
24. L. Pan, M. B. Sander, X. Huang, J. Li, M. R. Smith, E. W. Bittner, B. C. Bockrath and J. K. Johnson, *J. Am. Chem. Soc.*, 2004, **126**, 1308–1309
25. M. R. Palacin, *Chem. Soc. Rev.*, 2009, **38**, 2565–2575.
26. U. S Department of Energy, Technical Plan -Storage (2012)  
[www1.eere.energy.gov/hydrogenandfuelcells/mypp/pdfs/storage.pdf](http://www1.eere.energy.gov/hydrogenandfuelcells/mypp/pdfs/storage.pdf)
27. D. J. Cuscueta, A. A. Ghilarducci and H. R. Salva, *Inter. J. Hydro. Energy*, 2010, **35**, 11315–11323.
28. S. Q. Shi, C. Y. Ouyang and M. S. Lei, *J. Power Sources* 2007, **164**, 911–915.
29. Y. F. Liu, H. G. Pan, M. X. Gao, Y. F. Zhu, Y. Q. Lei and Q. D. Wang, *Electrochim. Acta* 2004, **49**, 545–555.
30. Y. Wang and M. Zhao, *J. Int. J. Hydrog. Energy* 2012, **37**, 3276–3282.
31. C. Wan, H. Yan, X. Ju, Y. Wang, M. Huang, F. Kong and W. Xiong, *J. Int. J. Hydrog. Energy* 2012, **37**, 13234–13242.
32. M. Y. Song, D. Ahn, I.H. Kwon and S. H. Chough, *J. Electrochem. Soc.* 2001, **148**, A1041–A1044
33. H. Yukawa, Y. Takahashi and M. Morinaga, *J. Comput. Mater. Sci.* 1999, **14**, 291–294.
34. Y. Zhu, Y. Yang, L. Wei, Z. Zhao and L. Li, *J. Alloy. Compd.* 2012, **520**, 207–212.
35. H. Zhang, N. Li, K. Li and D. Xue, *Acta Crystallographica B: Structural Science*, 2007, **63**, 812–818.

36. T. Esaka, H. Sakaguchi and S. Kobayashi, *Solid State Ionics*, 2004, **166**, 351–357.
37. G. Deng, Y.G. Chen, M.D. Tao, C.L. Wu, X.Q. Shen and H. Yang, *Electrochim. Acta* 2009, **54**, 3910–3914.
38. G. Deng, Y.G. Chen, M.D. Tao, C.L. Wu, X.Q. Shen and M. Liu, *Int. J. Hydrogen Energy* 2009, 34, 5568–5573.
39. A. Kaabi, M. Tliha, A. Dhahri, C. Khaldi, J. Lamloumi, *Ceramics International* 2016, **42**, 11682–11686.
40. G. Deng, Y.G. Chen, M.D. Tao, C.L. Wu, X.Q. Shen, H. Yang and M. Liu, *Electrochim. Acta* 2010, **55**, 1120–1124.
41. G. Deng, Y.G. Chen, M. D. Tao, C.L. Wu, X.Q. Shen, H. Yang and M. Liu, *Electrochim. Acta* 2010, 55, 884–886.
42. J. L. Tejuca, J. L. G. Fierro, *Properties and Applications of Perovskite-Type Oxides*, Marcel Dekker, New York, 1993.
43. K. Rida, A. Benabbas, F. Bouremmad, M. A. Pena and A. Martinez-Arias, *Catal. Commun.* 2006, **7**, 963–968.
44. D. Gang, C. Yungui, T. Mingda, W. Chaoling, S. Xiangqian, Y. Heng and Z. Ding, *Acta Chim. Sin.*, 2009, **67**, 2001–2004.
45. T. K. Mandal, L. Sebastian, J. Gopalakrishnan, L. Abrams and J. B. Goodenough, *Mater. Res. Bull.*, 2004, **39**, 2257–2264.
46. Y-H. Chen, B-W. Zhang, L. Yang, M-L. Zhang, C-R. Zhang, L. Kang and Y-C. Luo, *J. Nanomater.* 2014, **2014**, 1–8.
47. P. Hohenberg and W. Kohn, *Phys. Rev.*, 1964, **136**, B864.
48. W. Kohn and L. J. Sham, *Phys. Rev.*, 1965, **140**, A1133.
49. P. Giannozzi, S. Baroni, N. Bonini, M. Calandra, R. Car, C. Cavazzoni, D. Ceresoli, G. L. Chiarotti, M. Cococcioni, I. Dabo, A. D. Corso, S. de Gironcoli, S. Fabris, G. Fratesi, R. Gebauer, U. Gerstmann, C. Gougoussis, A. Kokalj, M. Lazzeri, L. Martin-Samos, N. Marzari, F. Mauri, R. Mazzarello, S. Paolini, A. Pasquarello, L. Paulatto, C. Sbraccia, S. Scandolo, G. Sclauzero, A. P. Seitsonen, A. Smogunov, P. Umari and R. M. Wentzcovitch, *J. Phys.: Condens. Mater* 2009, **21**, 395502.
50. H. J. Monkhorst and J. D. Pack, *Phys. Rev. B* 1976, **13**, 5188–5192.
51. R. Fletcher, *Practical Methods of Optimization, Second Edition*, John Wiley & Sons, Ltd, 1987.
52. A. Kokalj and M. Causa, *Proceedings of High Performance Graphics Systems and Applications European Workshop*, Bologna, Italy 2000, 51–54.

53. A. Kokalj, *J. Mol. Graphics Modelling* 1999, **17**, 176–179.
54. G. W. Watson, E. T. Kelsey, N. H. de Leeuw, D. J. Harris, and S. C. Parker, *J. Chem. Soc., Faraday Trans.* 1996, **92**, 433–438.
55. G. Wulff, *Z. Kristallogr. Mineral.* 1901, **34**, 449–530.
56. J. W. Gibbs, In *Collected Works*; Longman: New York, 1928.
57. S. W. Benson, *J. Chem. Educ.*, 1965, **42**, 502–18.
58. P.-O. Löwdin, *J. Chem. Phys.* 1950, **18**, 365
59. G. Bruhn, E. R. Davidson, I. Mayer and A. E. Clark, *Int. J. Quantum Chem.*, 2006, **106**, 2065–2072.
60. S. M. Selbach, J. R. Tolchard, A. Fossdal and T. Grande, *J. Sol. Sta. Chem.*, 2012, **196**, 249–254.
61. C. Boekema, P. C. Jonker, G. Filoti and F. Van Der Woude, *Hyperfine Inter.* 1979, **7**, 45–60.
62. L. Liu, A. Han, M. Ye and M. Zhao, *Sol. Energy Mater. & Sol. Cells* 2015, **132**, 377–384.
63. W. C. Koehler and E. O. Wollan, *J. Phys. Chem. Solids* 1957, **2**, 100–106.
64. D. Gryaznov, S. Baumann, E. A. Kotomin and R. Merkle, *J. Phys. Chem. C*. 2014, **118**, 29542–29553.
65. A. M. Ritzmann, A. B. Munoz-Garcia, M. Pavone, J. A. Keith and E. A. Carter, *Chem. Mater.* 2013, **25**, 3011–3019.
66. L. Wang, T. Maxisch and G. Ceder, *Phys. Rev. B*. 2006, **73**, 195107
67. M. Marezio and P. D. Dernier, *Mat. Res. Bull.* 1971, **6**, 23–30.
68. F. I. Bottin, F. Finocchi and C. Noguera, *Phys. Rev. B*. 2003, **68**, 035418
69. R. I. Eglitis and D. Vanderbilt, *Phys. Rev. B*. 2007, **76**, 155439
70. E. Heifets, J. Ho and B. Merinov, *Phys. Rev. B*. 2007, **75**, 155431
71. K. Johnston, M. R. Castell, A. T. Paxton and M. W. Finnis, *Phys. Rev. B*. 2004, **70**, 085415
72. H. Kawanowa, H. Ozawa, M. Ohtsuki, Y. Gotoh and R. Souda, *Surf. Sci.* 2002, **506**, 87–92.
73. C. H. Lanier, J. M. Rondinelli, B. Deng, R. Kilaas, K. R. Poepelmeier and L. D. Marks, *Phys. Rev. Lett.* 2007, **98**, 086102.
74. J. L. Wohlwend, R. K. Behera, I. Jang, S. R. Phillpot and S. B. Sinnott, *Surf. Sci.* 2009, **603**, 873–880.

75. X. Liu, J. Hu, B. Cheng, H. Qin, M. Zhao and C. Yang, *Sens. Actuators B* 2009, **139**, 520–526.
76. R. Smoluchowski, *Phys. Rev.* 1941, **60**, 661.
77. U. Landman, R. N. Hill and M. Mostoller, *Phys. Rev. B.* 1980, **21**, 448
78. N. H. de Leeuw, J. A. L. Rabone, *CrystEngComm*, 2007, **9**, 1178.
79. N. Y. Dzade, A. Roldan and N. H. de Leeuw, *J. Chem. Phys.* 2016, **144**, 174704
80. N. Y. Dzade, A. Roldan and N. H. de Leeuw, *Phys. Chem. Chem. Phys.*, 2016, **18**, 32007–32020.
81. G. J. Kubas, *Proceedings of the National Academy of Sciences of the United States of America* 2007, **104**, 6901–6907.
82. P. W. Atkins, T. L. Overton, J. P. Rourke, M. T. Weller and F. A. Armstrong, *Oxford University Press* 2010, ISBN 978–1–42–921820–7, p. 289
83. D. Sanchez-Portal, E. Artacho and J. M. Soler, *Solid State Commun.* 1995, **10**, 685–690
84. J. Hoffmann, S. Schnittger, J. Norpoth, S. Raabe, T. Kramer and C. Jooss, *J. Mater. Res.* 2012, **27**, 1462–1470.
85. R. Z. Huang and Y. M. Wang, *Phys. Stat. Sol. (a)* 2008, **205**, 1132–1138.
86. S. Hong and C. L. Fu, *Phys. Rev.* 2002, **66**, 094109.